Melt migration through the oceanic lower crust: a constraint from melt percolation modeling with finite solid diffusion

Jun Korenaga [*,1], Peter B. Kelemen

Department of Geology and Geophysics, Woods Hole Oceanographic Institution, Woods Hole, MA 02543, USA

Abstract

We present a melt percolation model incorporating finite solid diffusion to provide a quantitative constraint on how melt migrates through the oceanic lower crust at fast-spreading ridge axes. The lower crustal, layered gabbro in the Oman ophiolite, which was formed at a fast-spreading ridge, shows correlated variations in primary mineral compositions with a vertical wavelength less than 100–200 m. Possible effects of porous melt flow on these compositional variations are considered. The results of our numerical modeling indicate that melt transport by porous flow must be less than a few percent of the total incoming melt flux from the sub-ridge mantle, in order to preserve the observed correlations between different mineral compositions. It is also shown that rapid damping of compositional variations due to finite solid diffusion is likely, further reducing the potential role of porous flow melt transport. The dominant mode of melt migration through the oceanic lower crust must be more focused than pervasive porous flow, such as ascent in melt-filled fractures. © 1998 Elsevier Science B.V. All rights reserved.

Keywords: mid-ocean ridges; oceanic crust; magmas; melts; numerical models

1. Introduction

While studies of mid-ocean ridges during the past decade have dramatically improved our understanding of the genesis of the oceanic crust, the mechanism of formation of the oceanic lower crust is still elusive. Though mid-crustal, axial magma chambers are common at fast-spreading ridges (e.g. [1]), magma transport from the mantle to the magma chamber is not fully understood. Though this is un-

certain, a significant part of the lower crustal gabbro is believed to be modally layered on the basis of ophiolite studies. In this paper, we show that mineral chemistry of layered gabbro in the Oman ophiolite provides a strong constraint on the mode of melt migration through the lower crust.

The layered gabbro in the Oman ophiolite is thought to have formed at a fast-spreading ridge [2,3]. The origin of the layering has been controversial. The layered gabbro was once considered to represent basal crystallization at a huge magma chamber occupying almost the whole axial lower crust, with a lateral extent of >10 km [4–6]. This model was later rejected based on seismic evidence for a small-scale magma chamber beneath mid-ocean ridges (<100 m

* Corresponding author. Tel: +1 (508) 289-2464; Fax: +1 (508) 457-2150; E-mail: korenaga@mit.edu
[1] Also at MIT/WHOI Joint Program, Massachusetts Institute of Technology, Rm 54-521, Cambridge, MA 02139, USA.

thick and <2 km wide) (e.g. [7–9]), and a new class of model for crustal genesis has been advocated in which the lower crust is filled by downward ductile flow of gabbro crystallized in the mid-crustal magma chamber [10–12]. Although the ductile flow models attribute some of the layering in the lower gabbro to strong shear strain resulting from flow deflection near the base of crust, most or all of the observed layering is modal, not mechanical. In the context of the ductile flow model, therefore, the modal layering should originate in some crystallization processes within the magma chamber.

One difficulty of the ductile flow model is that it predicts extreme shear strain near the base of crust though such strong strain is not observed in the layered gabbros. Lubrication by interconnected melt along grain boundaries may enable strong shear deformation without substantial intragrain deformation [13]; at the same time, melt migration within the lower crust must take place as diffuse porous flow. The oceanic lower crust at fast spreading ridges is characterized by a relatively low seismic velocity [14,15] and high seismic attenuation [16], both of which probably indicate the existence of partial melt. Thus, diffuse porous flow may be realistic if partial melt is interconnected.

The Oman lower crustal gabbro shows not only modal layering but also compositional variations within olivine, clinopyroxene, and plagioclase [6]. The observed variations are correlated within and between mineral phases (Fig. 1). The compositional variations in the lower crustal gabbros must have been a primary signature imprinted upon crystallization, not a result of secondary reactions involving trapped liquid, because no significant crystal zoning is observed within all minerals, including plagioclase whose diffusion rates are extremely slow [17,18]. Therefore, the formation of the compositional variations must have been coeval with crystallization of the primary minerals and formation of the modal layering. Any crustal genesis model must be able to explain the preservation of the compositional variations as well as the formation of the modal layering. A corollary of the ductile flow model would be that modally layered gabbro with compositional variations crystallizes from the magma chamber, and that it flows downward interacting with a melt phase pervasively migrating along grain boundaries. If melt percolated

through the layered gabbro, however, the observed correlations between mineral compositions might be destroyed by the chromatographic effect of porous flow. Assuming instantaneous local equilibrium between the melt and the solid matrix, the advection velocity for the concentration of a certain element may be expressed as [19]:

$$w_c = Fw \tag{1}$$

where w is the melt advection velocity, and

$$F = \left[\frac{1 - \phi}{\phi} \frac{\rho_s}{\rho_f} K + 1 \right]^{-1}. \tag{2}$$

ϕ, ρ_s, ρ_f, and K are the porosity, the densities of the solid and the melt, and the solid/melt partition coefficient, respectively. The concentrations of chemical species with different partition coefficients migrate at different velocities.

The incoming melt flux at the Moho ($w\phi$) can be estimated from the crustal production rate as [20]:

$$w\phi = \frac{H_C V}{W_V \chi}, \tag{3}$$

with the duration time of melt migration of $W_V/(2V)$, where H_C, V, W_V, and χ are crustal thickness, full spreading rate, width of the neovolcanic zone, and the volume proportion of melt transport conduits within mantle peridotite, respectively. Assuming that melt migration is distributed within a 2-km-wide neovolcanic zone (i.e. $\chi = 1$ and $W_V = 2 \times 10^3$ m), the melt flux is on the order of 10^{-8} m/s during 2×10^4 years, for a half spreading rate of 1.6×10^{-9} m/s (or 50 mm/yr) and 6-km-thick crust. Incompatible elements (e.g. Mn in olivine) would migrate more rapidly than compatible elements (e.g. Ni in olivine), and the difference between the migrated distances would become more pronounced as time proceeds. Assuming instantaneous local equilibrium, a differential distance of migration for an incompatible element ($K = 0.5$) and a compatible element ($K = 5$) is calculated as a function of time (Fig. 2a). Since the observed compositional variations have a characteristic wavelength less than or equal to 100–200 m, correlated chemical variations would be obscured if the differential distance exceeds ∼100 m (Fig. 2b). For a plausible duration of melt migration (∼10^4 yr), therefore, the
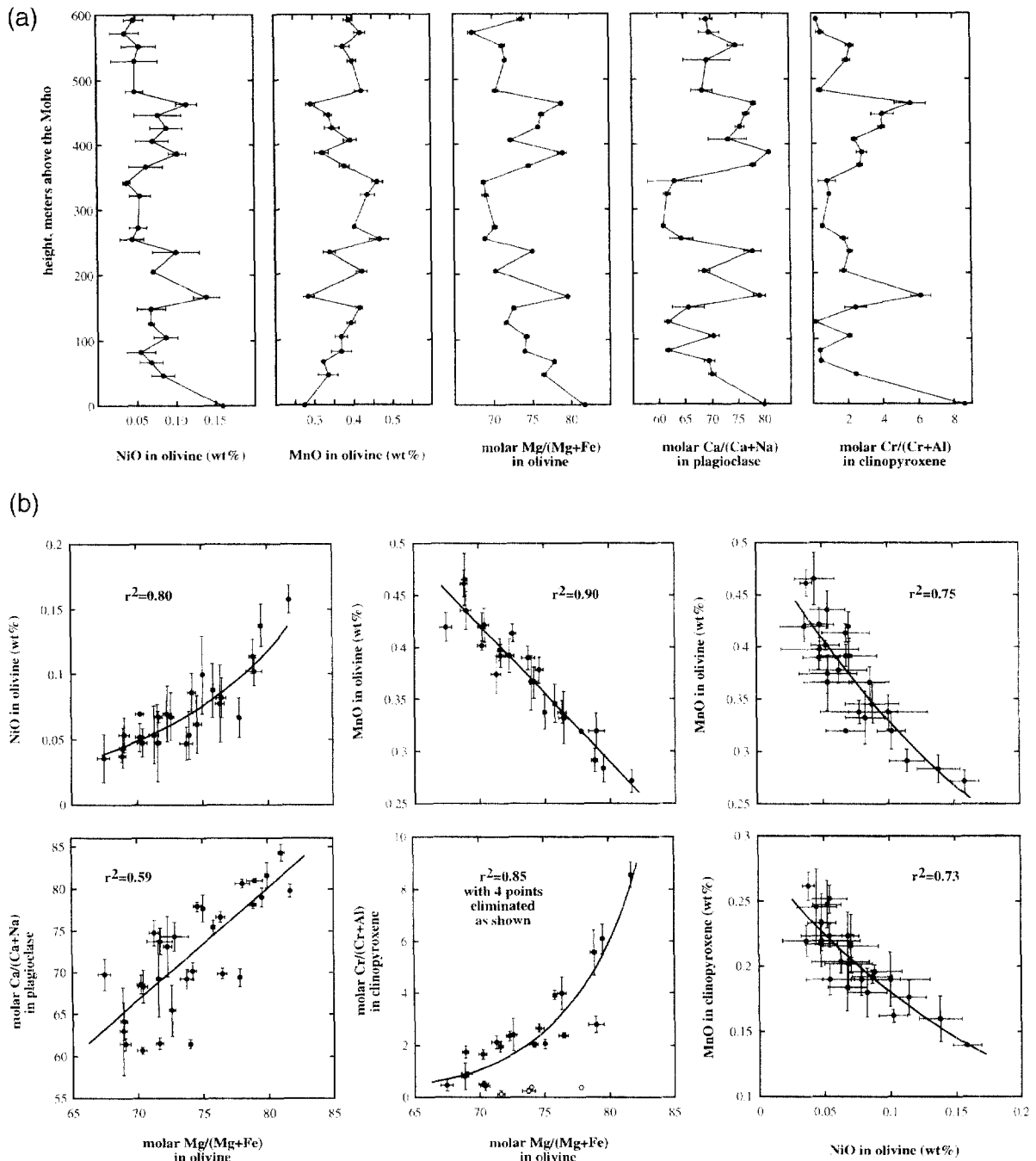
Fig. 1. (a) Compositional variations in Oman layered gabbro are plotted as a function of stratigraphic height. Data are taken from [6,31]. (b) NiO in olivine, MnO in olivine, molar Ca/(Ca + Na) in plagioclase ('An'), and molar Cr/(Cr + Al) in clinopyroxene are plotted as a function of molar Mg/(Mg + Fe) in olivine ('Fo'). Also, MnO in olivine and clinopyroxene are plotted as a function of NiO in olivine. All fits are exponential curves except for An vs. Fo and MnO in olivine vs. Fo, which are linear.
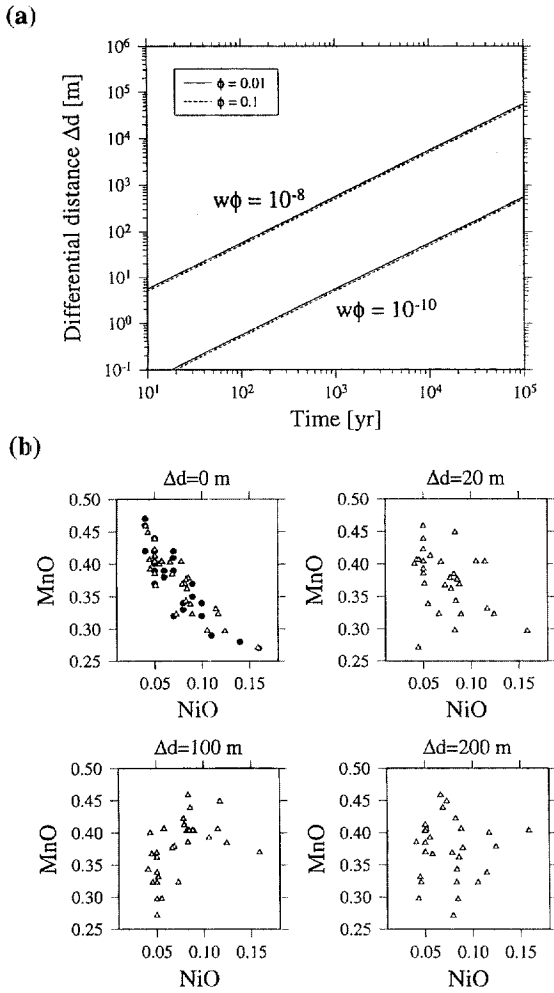
(a)

(b)

Fig. 2. (a) Differential distance of migration (Δd) between compatible ($K = 5$) and incompatible ($K = 0.5$) elements is plotted as a function of time. Melt flux $w\phi$ of 10^{-8} m/s corresponds to the estimated incoming melt flux from the mantle beneath a fast-spreading ridge axis. From Fig. 1, it is necessary that correlated chemical variations on the scale of 100 m be preserved over times of at least 10^4 years. (b) Effect of differential distance on the correlation between the NiO and MnO contents of olivine. To simulate this effect, NiO and MnO contents are first interpolated at 20-m intervals (shown as open triangles) from the original data (shown as solid circles). Then the interpolated NiO and MnO profiles are shifted by 20, 100, and 200 m, assuming periodic boundaries at the top and bottom. The correlation between NiO and MnO drastically deteriorates as the differential distance increases.

melt flux by porous flow must be less than 10^{-10} m/s ($<1\%$ of incoming melt flux) to preserve the observed correlations (Figs. 2 and 3).

The above argument, however, may depend on the validity of the assumption of instantaneous local equilibrium between the melt and the solid. For example, the solid diffusion time scale for an olivine grain with a radius of 2 mm is approximately 100 years at 1200°C (e.g. [21]), which may not be treated as 'instantaneous' for a certain range of melt advection time scales. To investigate this, it is necessary to solve a more complete set of diffusion–advection equations that include the effect of solid diffusion within porous media. Although similar sets of equations have been studied by other authors (e.g. [22–29]), our primary interest is to illuminate the effect of melt percolation on pre-existing chemical variations in solid concentrations, with finite solid diffusion rates.

2. Model formulation

For one-dimensional melt percolation through porous media with cylindrical symmetry (Fig. 4), mass conservation of an element in the melt may be expressed as (e.g. [22,27]):

$$\frac{\partial C_f}{\partial t} + w\frac{\partial C_f}{\partial z} = -\frac{2(1-\phi)\rho_s}{R\phi\rho_1}D_s\frac{\partial C_r}{\partial r}\bigg|_{r=R} \tag{4}$$

$$= -\frac{2(1-\phi)\rho_s}{R^2\phi\rho_1}\frac{\partial}{\partial t}\int_0^R C_r r\,dr \tag{5}$$

and mass conservation of an element within the stationary solid matrix ($0 \le r \le R$) may be written as:

$$\frac{\partial C_r}{\partial t} = D_s\left(\frac{\partial^2 C_r}{\partial r^2} + \frac{1}{r}\frac{\partial C_r}{\partial r}\right) \tag{6}$$

where C_f and C_r are the concentrations by weight of an element in the melt and the solid, respectively, R is the grain radius, and D_s is the solid diffusion rate. Chemical diffusion in the z-direction is neglected for both the melt and the solid phases because diffusion in the z-direction through the melt and the solid is insignificant for the time scale and wavelengths of interest (e.g. [20]). Eq. 5 instead of Eq. 4 is used for our calculation because the numerical evaluation of the integral is more accurate than the evaluation of $\partial C_r/\partial r$ at $r = R$ [22]. Chemical equilibrium is
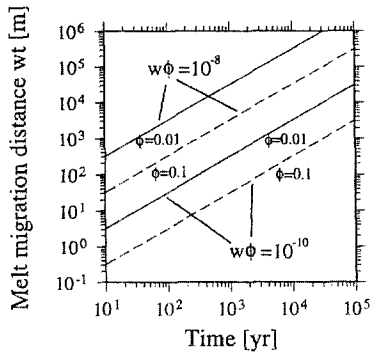
assumed to be attained at the melt/solid interface:

$$C_r(t, z, R) = K C_f(t, z). \qquad (7)$$

We employ a Gaussian-type initial concentration profile in the melt, i.e.

$$C_f(0, z) = \exp\left[-\frac{\left(z - \frac{2}{3}\lambda\right)^2}{\left(\frac{1}{3}\lambda\right)^2} \right] \qquad (8)$$

to represent a variation with a wavelength of λ. The
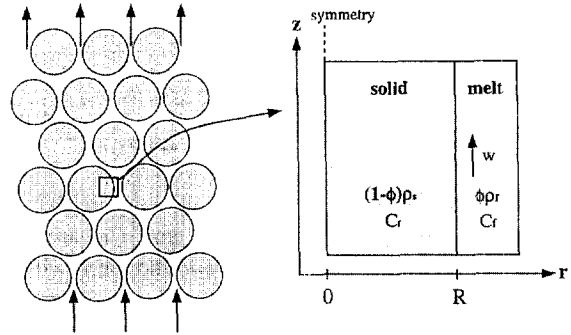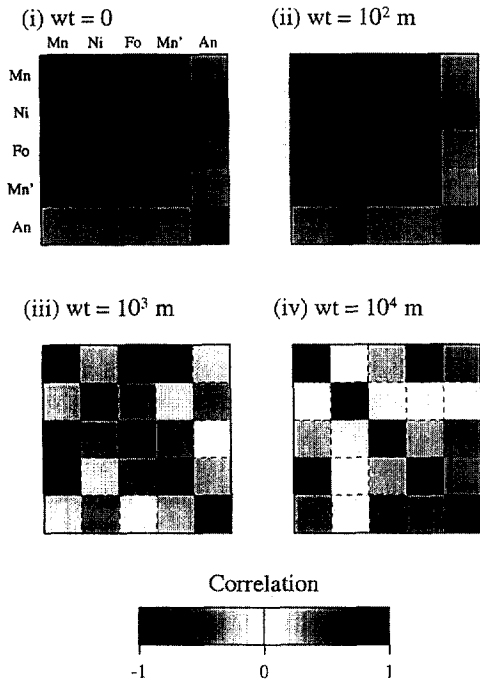
(a)

(b)

Correlation

Fig. 4. A one-dimensional melt percolation model. ϕ = porosity; ρ_s = density of solid; ρ_f = densities of melt; C_r = concentration of an element in solid; C_f = concentration of an element in melt; w = melt advection velocity; R = the representative size of solid grains in the r-direction.

solid matrix is at local equilibrium with the melt at $t = 0$, i.e.

$$C_r(0, z, r) = K C_f(0, z). \qquad (9)$$

Other boundary conditions include

$$\left. \frac{\partial C_r(t, z, r)}{\partial r} \right|_{r=0} = 0 \qquad (10)$$

due to cylindrical symmetry, and

$$C_r(t, 0, r) = K \exp(-4) \qquad (11)$$

to match the initial condition (Eq. 8) at the base of the model.

Fig. 3. A more quantitative demonstration of the chromatographic effect on correlated compositional variations. (a) Melt migration distance as a function of time for different total incoming melt fluxes. For full melt flux (10^{-8} m/s), total melt migration distance can be as large as 10^6 m. (b) Correlation matrix for Mn, Ni, and molar Mg/(Mg + Fe) in olivine (denoted as Fo), Mn in cpx (Mn'), and molar Ca/(Ca + Na) in plagioclase (An), calculated at different melt migration distances. Bulk partition coefficients for different chemical species are estimated using the average volume or weight proportion of the primary minerals reported by Browning [31] and partition coefficients appropriate for 1200°C and 2 kbar [34–36]. Using 2% porosity, F in Eq. 2 is then calculated as $F_{Mn} = 0.039$, $F_{Ni} = 0.005$, $F_{Fe} = 0.060$, and $F_{Mg} = 0.017$. We do not migrate plagioclase composition at all, considering its extremely slow solid diffusion [17,18]. As in Fig. 2b, periodic boundaries are used at the top and bottom, and concentration profiles are resampled every 20 m to calculate correlation coefficients. Spearman's non-parametric correlation coefficients are calculated instead of linear correlation coefficients, because the former provide a more robust estimate of correlation for noisy data (e.g. [37]).

The above equations are normalized with

$$t' = \frac{t}{H/w}, \quad z' = \frac{z}{H}, \quad r' = \frac{r}{R},$$

$$C_r' = \frac{C_r}{C_{s0}}, \quad C_f' = \frac{C_f}{C_{f0}} \tag{12}$$

where H is a vertical dimension of the percolation system (set as $H = 3\lambda$), and C_{s0} and C_{f0} are the initial concentrations in the solid and the melt, which are at equilibrium as $C_{s0} = KC_{f0}$. After dropping primes, the non-dimensionalized equations are

$$\frac{\partial C_f}{\partial t} + \frac{\partial C_f}{\partial z} = -2K_e \frac{\partial}{\partial t} \int_0^1 C_r r \, dr \tag{13}$$

$$\frac{\partial C_r}{\partial t} = \mathrm{Da} \left(\frac{\partial^2 C_r}{\partial r^2} + \frac{1}{r} \frac{\partial C_r}{\partial r} \right) \tag{14}$$

with the following boundary and initial conditions:

$$C_r(t, z, R) = C_f(t, z) \tag{15}$$

$$\left. \frac{\partial C_r(t, z, r)}{\partial r} \right|_{r=0} = 0 \tag{16}$$

$$C_r(t, 0, r) = \exp(-4) \tag{17}$$

$$C_f(0, z) = \exp\left[-(9z - 2)^2 \right] \tag{18}$$

$$C_r(0, z, r) = C_f(0, z) \tag{19}$$

where

$$K_e = \frac{1 - \phi}{\phi} \frac{\rho_s}{\rho_f} K \tag{20}$$

$$\mathrm{Da} = \frac{\tau_{ma}}{\tau_{sd}} = \frac{H/w}{R^2/D_s}. \tag{21}$$

K_e is the effective partition coefficient, Da is the diffusion-controlled Damkohler number, and τ_{ma} and τ_{sd} are the melt advection time scale and the solid diffusion time scale, respectively. The Damkohler number generally measures the relative importance of solid–liquid reaction to fluid advection. In this problem, the reaction rate is controlled by solid diffusion. We further applied a Boussinesq-type approximation and omitted the ρ_s/ρ_f term in Eq. 20. The above set of equations are solved numerically using the Crank–Nicolson algorithm (e.g. [30]). The grid sizes are 0.01 for the z-direction and 0.02 for the r-direction.

The above formulation is only an approximation for melt percolation through porous media composed of several different minerals. To precisely model melt percolation through a mineral aggregate, such as gabbro, mass conservation in the melt must describe mass transfer between melt and multiple solid phases. In addition, mass conservation within the solid matrix needs to be described by a set of multiple solid diffusion equations. Since all grain boundaries are assumed to be lubricated with the melt phase, however, the fastest solid diffusion among different minerals dominates the mass transfer between the melt and the solid. Diffusion rates in olivine are, in general, more than an order of magnitude larger than diffusion rates in clinopyroxene and plagioclase (e.g. [21]). For the case of Ni or Mn diffusion, for example, Eq. 13 is approximately valid if K_e is properly scaled to reflect olivine mass proportion (i.e. 12% for the Oman layered gabbro [31]), and the diffusion process in solid can be described by Eq. 14 using diffusion rates in olivine.

3. Results

Since we are interested in possible migration of a compositional variation with a wavelength of ~100 m, the vertical dimension of the system is set as 300 m, sufficiently long to observe the chemical advection and diffusion of an initial 100-m-wide Gaussian-type concentration profile. The grain radius is set at 2 mm, a characteristic grain size reported by Browning [6]. Possible ranges of the controlling parameters, K_e and Da, are then estimated for diffusion in olivine and plagioclase, and K_e is varied from 10^{-1} to 10^3 and Da from 10^{-5} to 10^3 (Fig. 5).

Three distinct behaviors of the system are identified for different combinations of K_e and Da. To illustrate them, examples of the results of numerical calculations are shown in Fig. 6 for the cases of Da $= 10^{-2}$, 1, and 10^2, all with $K_e = 1$. For rapid solid diffusion (Da $= 10^2$; Fig. 6a), instantaneous local equilibrium is almost achieved; the solid concentration profile simply follows the analytical solution of Eq. 1. For slow solid diffusion (Da $= 10^{-2}$: Fig. 6b), the solid concentration only follows the advecting melt composition at the crystal/liquid interface, and zoning in the grains gradually develops as time pro-
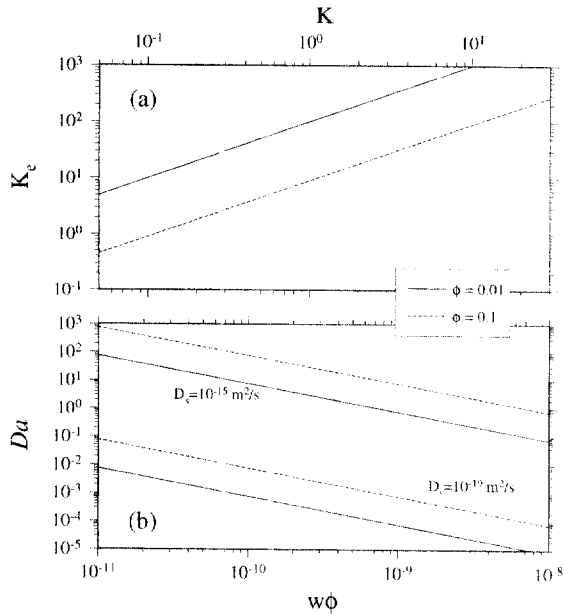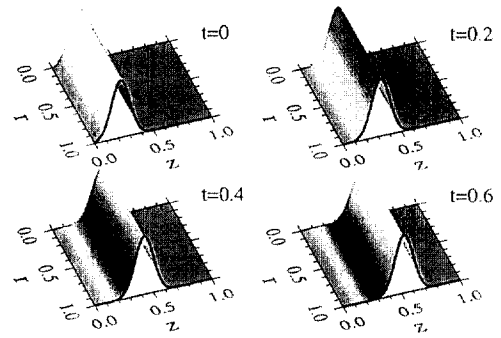
Fig. 5. (a) Effective partition coefficient K_c (Eq. 20) for two porosities ($\phi = 0.01$ and 0.1) is plotted as a function of partition coefficient. (b) Diffusion-controlled Damkohler number (Da; Eq. 21) is plotted as a function of melt flux, $w\phi$. Grain radius R and system dimension H are fixed as 2 mm and 300 m, respectively, and matrix porosity is fixed as 0.01 (solid line) or 0.1 (dashed line). A solid diffusion rate of 10^{-15} m²/s corresponds to Ni diffusion or Fe–Mg interdiffusion in olivine at 1200°C [21], and solid diffusion rate of 10^{-19} m²/s corresponds to NaSi–CaAl interdiffusion in plagioclase under H₂O saturated conditions [18]. Solid diffusion in plagioclase would be much slower (e.g. 10^{-21} m²/s) under dry conditions [17].

Fig. 6. Examples of numerical calculations are shown for $K_c = 1$. Thick curve at $r = 1$ denotes the analytical solution by Eq. 1. (a) A case of rapid solid diffusion; Da $= 10^2$. (b) A case of slow solid diffusion; Da $= 10^{-2}$. (c) A case of intermediate solid diffusion; Da $= 1$.
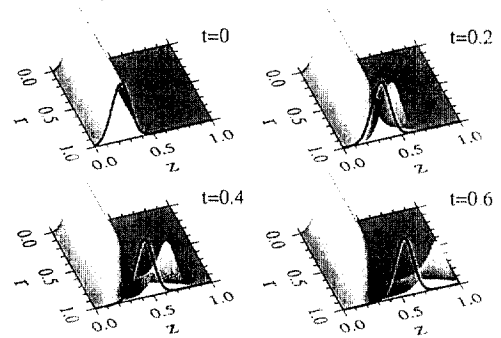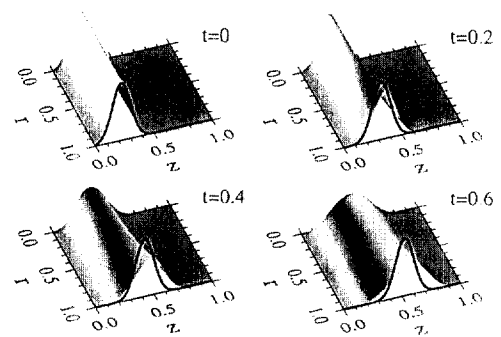
ceeds. When the melt advection time scale is equal to the solid diffusion time scale (Da $= 1$; Fig. 6c), although solid concentration can migrate as fast as the analytical solution predicts, rapid damping of the initial variation in concentration in the z-direction is observed. This is because the diffusion response of the solid phase to the melt advection is not fast enough to avoid the development of a concentration gradient within a grain.

The results of numerical calculations are summarized in Fig. 7. The grain-average migration rate of solid concentration is compared to the analytical solution from Eq. 1, and the percentage difference of these two migration rates is plotted as a function of Da (Fig. 7a). For Da ≥ 1, solid concentration can migrate as fast as the analytical solution pre-

dicts. The percentage delay is less than 50% for a range of Da applicable to diffusion in olivine. On the other hand, the plagioclase composition can hardly migrate because of slow diffusion rates (Da $< 10^{-2}$).
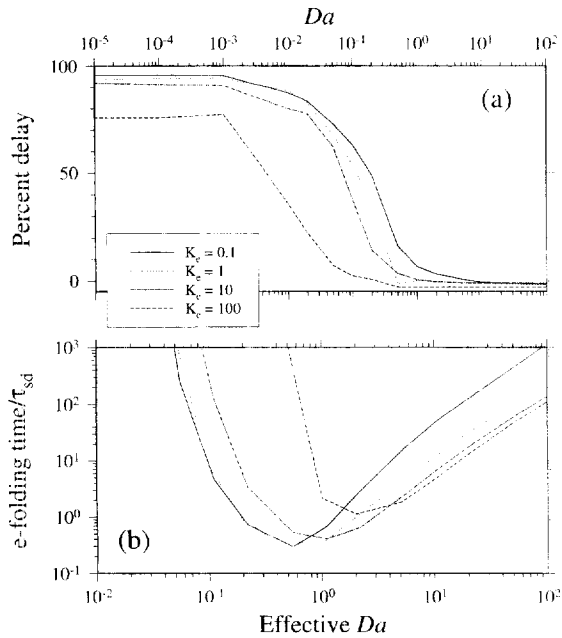
Fig. 7. (a) Grain-average percentage delay with respect to the analytical solution (Eq. 1) is plotted as a function of Da. (b) e-folding time scale, of chemical variation normalized to solid diffusion time scale (τ_{sd}), is plotted as a function of effective Da (see text).

A damping time scale, or e-folding time scale (over which the amplitude of compositional variation decreases by $1/e$), is plotted as a function of effective Da (defined as Da$/F$ or Da($K_e + 1$)), which is the chemical advection time scale (τ_{ma}/F; as predicted by Eq. 1) scaled by the solid diffusion time scale (Fig. 7b). When the chemical advection time scale is of the same order of the solid diffusion time scale, the e-folding time scale is close to the solid diffusion time scale and the amplitude of compositional variation decreases most rapidly.

It is interesting to note a close relationship between our modeling results and the analytic solution of a similar advection–diffusion problem [24,26]. Kenyon [24] and Spiegelman and Kenyon [26] considered the effect of solid diffusion on time-varying chemical concentration of melt influx. The principal difference from our model is the initial and boundary conditions employed; whereas we are interested in the fate of pre-existing variations in solid concentration, they considered the fate of input variations in melt concentration. The model equations are essentially the same; the system is defined by the same two non-dimensional numbers, K_e and Da, which

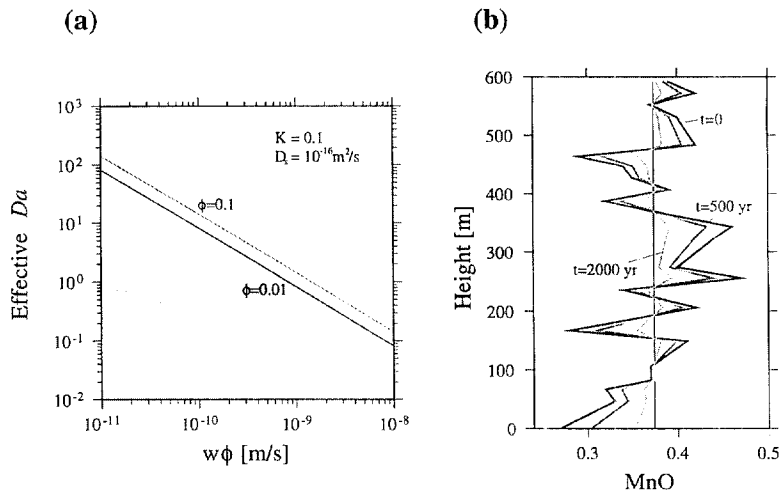
Fig. 8. (a) Effective Da plotted as a function of melt flux, $w\phi$, with a range of porosity from 0.01 to 0.1, and with $K = 0.1$ (scaled to reflect about 10% weight proportion of olivine) and $D_s = 10^{-16}$ m^2/s corresponding to Mn diffusion in olivine. (b) Effect of damping due to solid diffusion on the MnO content of olivine when effective Da is larger than 10^{-1} and lower than 10. The damping time scale is ~1300 years for Mn. The average value of compositional variation is used as the equilibrium concentration (shown as dashed line), and the initial deviation from the equilibrium concentration decreases as exp$(-t/\tau_e)$ where τ_e is the damping time scale. The blocky nature of the concentration profile even after damping reflects our point-wise damping calculation; because of the limited number of data points, we do not consider possible vertical blurring of variation. After 2000 years of melt migration, vertical variation of the MnO content in olivine would be hardly detectable.

a

lavas
dikes
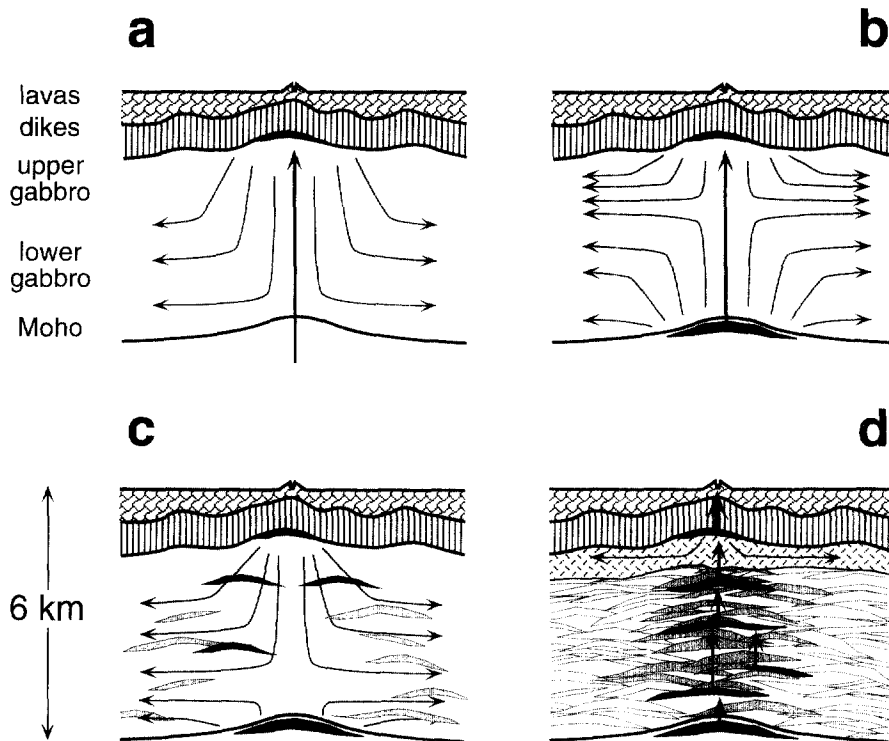upper
gabbro

lower
gabbro

Moho

b

c

6 km

d

Fig. 9. Schematic drawings for recently proposed crustal models. (a) Ductile flow model in its simplest form (e.g. [10–12,38]). Ductile flow down and outward from a mid-crustal axial magma chamber constructs the lower crust. (b) Ductile flow model incorporating a basal sill (e.g. [39]). (c) Hybrid ductile flow model with on- and off-axis sill intrusions (e.g. [40]). (d) 'Sheeted sill' model with melt transport by hydrofracture and in situ emplacement of the lower crust by on-axis sill intrusions (e.g. [32,33,41]).

are denoted by [26] as K' and $1/Pe$, respectively. Therefore, our results share the key behaviors of the system with their solution; for example, the transition from the equilibrium (i.e. zero percent delay) to the disequilibrium behavior of the system occurs around Da of 0.1–1 (compare our Fig. 7a with fig. 5 of [26]).

4. Discussion and conclusion

Since diffusion in olivine at 1200°C is well characterized by Da > 10^{-1} for a reasonable range of melt advection time scales (Fig. 5b), the differential distances of migration between compatible and incompatible elements are likely to be similar to the analytical prediction in Fig. 2. Therefore, the previous argument based on instantaneous local equilibrium is still valid; melt transport through the oceanic lower crust by pervasive porous flow cannot

be greater than a few percent of the total incoming melt flux to preserve the observed correlations between compositional variations in olivine.

The effective Da is plotted as a function of melt flux for Mn diffusion in olivine (Fig. 8). For a melt flux larger than 1% of the total melt flux through the oceanic lower crust, it is likely that the effective Da has a value close to 1. Therefore, damping of the amplitude of chemical variation takes place, on the time scale of solid diffusion. We note that, for a long-wavelength compositional variation such as is observed in the Oman layered gabbros, damping due to solid diffusion can take place much faster than the damping due to diffusion through the porous melt phase. To avoid the rapid damping of observed compositional variations, the contribution of porous flow to the melt transport has to be lower than 1% of the incoming flux, as required by preservation of correlated compositional variations.

Since we have assumed that all grain boundaries

are lubricated by melt phase, the observed grain size of ~2 mm controls the solid diffusion time scale, and thus the Damkohler number. The Damkohler number depends on grain size as R^{-2} (Eq. 21), and larger grain size or wider channel spacing is another way to preserve correlated compositional variations. The modeling result suggests that approximately 100 times larger channel spacing (~20 cm) would not destroy the correlation even with fast solid diffusion (10^{-15} m²/s) at the full melt flux of 10^{-8} m/s (Fig. 7a). For a mineral aggregate separated by such melt channels, the solid diffusion rate would be dominated by the slowest diffusion rate among different minerals, and therefore the destruction of correlation between different mineral compositions due to melt migration would be unlikely.

In summary, the results of this numerical experiment substantiate the results of our initial, analytical calculation with instantaneous local equilibrium; not only the correlated compositional variations, but also the existence of the variations themselves are strong evidence against diffuse porous flow of all melt from the mantle through the oceanic lower crust. The ductile flow models for oceanic lower crust formation (Fig. 9a–c) seem to require intercrystalline lubrication by an interconnected melt phase, and thus pervasive reaction with lower crust would be unavoidable for incoming melt. One may argue that the observed compositional variations could result from later, off-axis sill intrusion (Fig. 9c). This model is, however, inconsistent with seismic observations that support focus crustal accretion within a narrow (2–3 km) neovolcanic zone [1]. In addition, such off-axis, lower-crustal intrusions, located outside the high seismic attenuation zone [16], would probably have been observed by seismic reflection experiments. The formation mechanism of the lower crust, therefore, must incorporate more focused melt transport, such as the hydrofracture model proposed by Kelemen and his co-workers (Fig. 9d) [32,33].

Acknowledgements

References

[1] R.S. Detrick, P. Buhl, E. Vera, J. Mutter, J. Orcutt, J. Madsen, T. Brocher, Multichannel seismic imaging of a crustal magma chamber along the East Pacific Rise, Nature 326 (1987) 35–41.

[2] G.R. Tilton, C.A. Hopson, J.E. Wright, Uranium–lead isotopic ages of the Samail ophiolite, J. Geophys. Res. 86 (1981) 2763–2775.

[3] A. Nicolas, Structures of Ophiolites and Dynamics of Oceanic Lithosphere, Kluwer, Dordrecht, 1989.

[4] J.S. Pallister, C.A. Hopson, Samail ophiolite plutonic suite: field relations, phase variation, cryptic variation and layering, and a model of a spreading ridge magma chamber, J. Geophys. Res. 86 (1981) 2593–2644.

[5] J.D. Smewing, Mixing characteristics and compositional differences in mantle-derived melts beneath spreading axes: evidence from cyclically layered rocks in the ophiolite of North Oman, J. Geophys. Res. 86 (1981) 2645–2659.

[6] P. Browning, Cryptic variation within the Cumulate Sequence of the Oman ophiolite: magma chamber depth and petrological implications, in: Ophiolites and Oceanic Lithosphere, Geological Society of London, 1984, pp. 71–82.

[7] G.M. Kent, A.J. Harding, J.A. Orcutt, Evidence for a smaller magma chamber beneath the East Pacific Rise at 9°30′N, Nature 344 (1990) 650–653.

[8] D.R. Toomey, G.M. Purdy, S.C. Solomon, W.S.D. Wilcock, The three-dimensional seismic velocity structure of the East Pacific Rise near latitude 9°30′N, Nature 347 (1990) 639–645.

[9] J.M. Sinton, R.S. Detrick, Mid-ocean ridge magma chambers, J. Geophys. Res. 97 (1992) 197–216.

[10] J. Phipps Morgan, Y.J. Chen, The genesis of oceanic crust: magma injection, hydrothermal circulation, and crustal flow, J. Geophys. Res. 98 (1993) 6283–6297.

[11] T.J. Henstock, A.W. Woods, R.S. White, The accretion of oceanic crust by episodic sill intrusion, J. Geophys. Res. 98 (1993) 4143–4161.

[12] J.E. Quick, R.P. Denlinger, Ductile deformation and the origin of layered gabbro in ophiolites, J. Geophys. Res. 98 (1993) 14015–14027.

[13] A. Nicolas, C. Fraydier, M. Godard, A. Vauchez, Magma chambers at oceanic ridges: how large? Geology 21 (1993) 53–56.

[14] A.J. Harding, J.A. Orcutt, M.E. Kappus, E.E. Vera, J.C. Mutter, P. Buhl, R.S. Detrick, T.M. Brocher, Structure of young oceanic crust at 13°N on the East Pacific Rise from expanding spread profiles, J. Geophys. Res. 94 (1989) 12163–12196.

[15] E.E. Vera, J.C. Mutter, P. Buhl, J.A. Orcutt, A.J. Harding, M.E. Kappus, R.S. Detrick, T.M. Brocher, The structure of 0- to 0.2-m.y.-old oceanic crust at 9°N on the East Pacific Rise from expanded spread profiles, J. Geophys. Res. 95 (1990) 15529–15556.

[16] W.S.D. Wilcock, S.C. Solomon, G.M. Purdy, D.R. Toomey, The seismic attenuation structure of a fast-spreading mid-ocean ridge, Science 258 (1992) 1470–1474.

[17] T.L. Grove, M.B. Baker, R.J. Kinzler, Coupled CaAl–NaSi diffusion in plagioclase feldspar: experiments and applications to cooling rate speedometry, Geochim. Cosmochim. Acta 48 (1984) 2113–2121.

[18] M. Liu, R.A. Yund, NaSi–CaAl interdiffusion in plagioclase, Am. Mineral. 77 (1992) 275–283.

[19] D. McKenzie, The generation and compaction of partially molten rock, J. Petrol. 25 (1984) 713–765.

[20] J. Korenaga, P.B. Kelemen, Origin of gabbro sills in the Moho transition zone of the Oman ophiolite: implications for magma transport in the oceanic lower crust, J. Geophys. Res., in press.

[21] J.B. Brady, Diffusion data for silicate minerals, glasses, and liquids, in: T.J. Ahrens (Ed.), Mineral Physics and Crystallography: A Handbook of Physical Constants, American Geophysical Union, Washington, DC, 1995, pp. 269–290.

[22] O. Navon, E. Stolper, Geochemical consequences of melt percolation: the upper mantle as a chromatographic column, J. Geol. 95 (1987) 285–307.

[23] J.L. Bodinier, G. Vasseur, J. Vernieres, C. Dupuy, J. Fabries, Mechanisms of mantle metasomatism: geochemical evidence from the Lherz orogenic peridotite, J. Petrol. 31 (1990) 597–628.

[24] P.M. Kenyon, Trace element and isotopic effects arising from magma migration beneath mid-ocean ridges, Earth Planet. Sci. Lett. 101 (1990) 367–378.

[25] G. Vasseur, J. Vernières, J.L. Bodinier, Modeling of trace element transfer between mantle melt and heterogranular peridotite matrix, in: Orogenic Lherzolites and Mantle Process, J. Petrol. Spec. Publ., 1991, pp. 41–54.

[26] M. Spiegelman, P. Kenyon, The requirement for chemical disequilibrium during magma migration, Earth Planet. Sci. Lett. 109 (1992) 611–620.

[27] H. Iwamori, Melt–solid flow with diffusion-controlled chemical reaction, Geophys. Res. Lett. 19 (1992) 309–312.

[28] P.M. Kenyon, Trace elements in migrating high-temperature fluids: effects of diffusive exchange with the adjoining solid, J. Geophys. Res. 98 (1993) 22007–22020.

[29] M. Godard, J. Bodinier, G. Vasseur, Effects of mineralogical reactions on trace element redistributions in mantle rocks during percolation processes: a chromatographic approach, Earth Planet. Sci. Lett. 133 (1995) 449–461.

[30] W.F. Ames, Numerical Methods for Partial Differential Equations, Barnes and Nobles, 1969.

[31] P. Browning, The petrology, geochemistry, and structure of the plutonic rocks of the Oman ophiolite, Ph.D. thesis, The Open University, Milton Keynes, England, 1982.

[32] P.B. Kelemen, K. Koga, N. Shimizu, Geochemistry of gabbro sills in the crust/mantle transition zone of the Oman ophiolite: implications for the origin of the oceanic lower crust, Earth Planet. Sci. Lett. 146 (1997) 475–488.

[33] P.B. Kelemen, E. Aharonov, Periodic formation of magma fractures and generation of layered gabbros in the lower crust beneath oceanic spreading centers, in: Geophysical Monograph Series, American Geophysical Union, in press.

[34] P.L. Roeder, R.F. Emslie, Olivine–liquid equilibrium, Contrib. Mineral. Petrol. 29 (1970) 275–289.

[35] A.J. Irving, A review of experimental studies of crystal/liquid trace element partitioning, Geochim. Cosmochim. Acta 42 (1978) 743–770.

[36] C.H. Langmuir, E.M. Klein, T. Plank, Petrological systematics of mid-ocean ridge basalts: constraints on melt generation beneath ocean ridges, in: Mantle Flow and Melt Generation at Mid-Ocean Ridges, American Geophysical Union, 1992, pp. 183–280.

[37] W.H. Press, S.A. Teukolsky, W.T. Vetterling, B.P. Flannery, Numerical Recipes in C, 2nd edn. Cambridge University Press, New York, 1992.

[38] A. Nicolas, I. Reuber, K. Benn, A new magma chamber model based on structural studies in the Oman ophiolite, Tectonophysics 151 (1988) 87–105.

[39] H. Schouten, C. Denham, Virtual ocean crust, EOS Trans. AGU 76 (1995) 48.

[40] F. Boudier, A. Nicolas, B. Ildefonse, Magma chambers in the Oman ophiolite: fed from the top or the bottom? Earth Planet. Sci. Lett. 144 (1996) 239–250.

[41] J.H. Bedard, R.S.J. Sparks, R. Renner, M.J. Cheadle, M.A. Hallworth, Peridotite sills and metasomatic gabbros in the Eastern Layered Series of the Rhum Complex, J. Geol. Soc. Lond. 145 (1988) 207–224.